THE JOURNAL OF PHYSICAL CHEMISTRY C
A JOURNAL OF THE AMERICAN CHEMICAL SOCIETY

pubs.acs.org/JPCC

Article

Understanding Wavelength-Dependent Synergies between Morphology and Photonic Design in TiO_2-Based Solar Powered Redox Cells

Published as part of The Journal of Physical Chemistry C virtual special issue "Hot Electrons in Catalysis".

Jiaming Ma, Kiseok Oh, and Giulia Tagliabue*

Cite This: *J. Phys. Chem. C* 2023, 127, 11−21

Read Online

ACCESS | Metrics & More | Article Recommendations | Supporting Information

ABSTRACT: Solar powered redox cells (SPRCs) are promising for large-scale and long-term storage of solar-energy, particularly when coupled with redox flow batteries (RFBs). While efforts have primarily focused on heterostructure engineering, the potential of synergistic morphology and photonic design has not been carefully studied. Here, we investigate the wavelength-dependent effects of light-absorption and charge transfer characteristics on the performance of gold decorated TiO_2-based SPRC photoanodes operating with RFB-compatible redox couples. Through an in-depth optical and photoelectrochemical characterization of three complementary TiO_2 microstructures, namely nanotubes, honeycombs, and nanoparticles, we elucidate the combined effects of nanometer-scale semiconductor morphology and plasmonic design across the visible spectrum. In particular, thin-walled TiO_2 nanotubes exhibit a ∼ 50% increase in solar-to-chemical efficiency (STC) compared to thick-walled TiO_2 honeycombs thanks to improved charge transfer. Au nanoparticles both increase generation and interfacial charge transfer (above bandgap) and promote hot carrier injection (below bandgap) leading to a further 25% increase in STC. Overall, Au/TiO_2 nanotubes achieve a high photocurrent at 0.098 mA/cm^2 and an excellent STC of 0.06%, among the highest with respect to the theoretical limit. The incident photon to current efficiency and internal quantum efficiency are also superior to those of bare TiO_2 showing maximum values of 54.7% and 67%, respectively. Overall, nanophotonic engineering that synergistically combines morphology optimization and plasmonic sensitization schemes offer new avenues for improving rechargeable solar-energy technologies such as solar redox flow batteries.

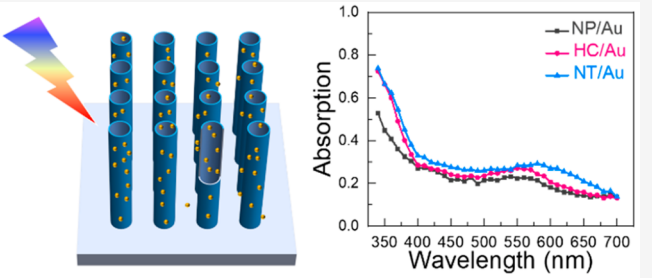

INTRODUCTION

The intermittent nature of solar energy challenges the power grid in terms of adequate energy storage capacity. Solar powered redox cells (SPRCs) have recently emerged as an all-in-one device that can realize simultaneously conversion and storage of solar energy.[1,2] Different from water splitting devices or conventional battery designs (e.g., Li-ion), SPRCs operate with redox couples that have fast reaction kinetics, do not require gas collection,[3] and enable the decoupling of power and energy storage.[4,5] Indeed, by storing the anolyte and catholyte into separate tanks, SPRCs can be easily converted into solar redox flow batteries thanks to the sharing of the same redox pairs[6,7] (Figure 1). This integration leads to tremendous advantages toward overcoming cost, reliability, and scalability issues of large-energy grid-storage applications.[8,9] Yet, cost-effective realization of SPRCs for redox flow batteries is challenged by the trade-off between solar to chemical efficiency (STC) and cell discharge voltage.[10]

Three main processes must be optimized for high STC: (i) light absorption and generation of electron−hole pairs; (ii) electron/hole transport, i.e., electron migration to the contact and hole migration to the electrode/electrolyte interface (photoanode); and (iii) reaction kinetics, including mass transport of redox couples to the interface.[1] Toward full use of the solar spectrum, semiconductors with narrow bandgap, including Si,[11] GaAs,[12] Ta_3N_5,[13] WSe_2,[14] CdSe,[15] Fe_2O_3,[16,17] and $MoSe_2$,[18] have been considered. However, the cell discharge voltage, theoretically defined by the potential difference between the redox couples,[19,20] must be smaller than the photoelectrode bandgap. Thus, wide-bandgap materials can open new opportunities toward high discharge voltage applications, while retaining ideal STCs as high as 10%.[21] To overcome this trade-off, narrow-bandgap dual-

Received: August 17, 2022
Revised: November 21, 2022
Published: December 16, 2022

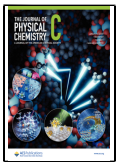

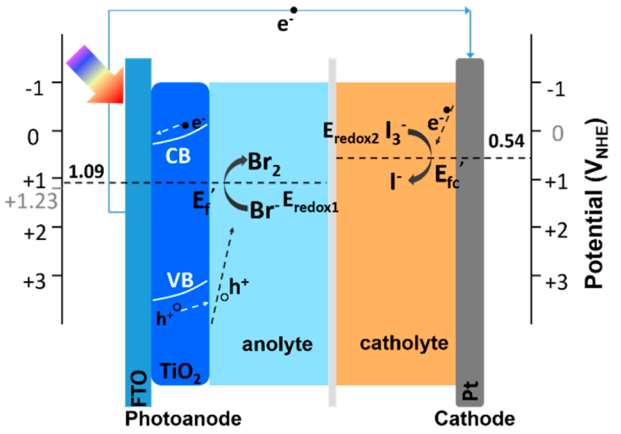

Figure 1. Schematic of a solar powered redox cell showing the main components and the important energy levels. Upon contact with the electrolyte, the Fermi level of TiO_2 and Pt aligns with the respective redox potentials, indicated by the dashed lines. The standard reduction potentials for $2H^+/H_2$, O_2/H_2O redox couples are marked with gray color. The band-bending at the TiO_2/anolyte interface is also depicted. Back-illumination is represented by the rainbow arrow.

photoelectrodes SPRC designs have been used.[13] Additionally, heterostructures[22] and PV-biased cells[12,23,24] have been successfully demonstrated. Yet, these solutions significantly increase the system complexity and/or its costs[6] and often require the introduction of extra protection layers against chemical corrosion and photocorrosion.[25] Thus, there remains an interest in improving the performance of single wide-bandgap semiconductor SPRCs.[6] In particular, TiO_2 has attracted significant attention thanks to its exceptional chemical stability[22] and favorable band-alignment for a wide range of redox couples.[19]

Contrary to photoelectrochemical systems, such as liquid-based hydrogen production,[26−33] dye-sensitized solar cells,[34−37] and CO_2 reduction,[38−42] SPRCs have not yet leveraged nanophotonic design strategies to improve STC. On one hand, plasmonic nanostructures, i.e., metallic nanoparticles supporting collective oscillations of the electron cloud,[43,44] exhibit exceptional and tunable light harvesting properties. Also, they enable the generation and control of strong electric-field enhancements at nanoscale dimensions,[45,46] enhancing light concentration and electron−hole pair generation in a supporting semiconductor.[47−49] Additionally, nonradiative decay of surface plasmons results in the generation of highly energetic electron/hole pairs in the metal (hot carriers), which can be transferred into an adjacent semiconductor (sensitization).[50,51] Thus, plasmonic nanostructures can improve STC both above and below the bandgap. On the other hand, microscale morphologies of the semiconductor catalyst can enhance light trapping while nanostructuring can introduce resonant (Mie) modes that maximize light absorption in ultrathin, subwavelength structures.[52] In this regard, it has been shown that TiO_2 nanotubes[53,54] and hollow nanospheres[55,56] have higher light absorption than nanoparticles due to enhanced scattering. Furthermore, by simultaneously enlarging the electrode−electrolyte interface as well as shortening the transport distance, micro-/nano-engineered designs can improve surface reaction kinetics and charge collection. Despite all these advantages, however, synergistic coupling of plasmonic and micro-/nano-structuring approaches in SPRCs has not been carefully investigated.

In this work, we leverage a unique combination of plasmonic and micro-/nano-engineering to optimize the performance of Au-decorated TiO_2 SPRCs photoanodes. Indeed, we study three complementary morphologies with increasing light harnessing and active surface area, namely TiO_2 nanoparticles (NP), TiO_2 honeycombs (HC), and TiO_2 nanotubes (NT, Figure 2a). Importantly, a complete characterization of optical

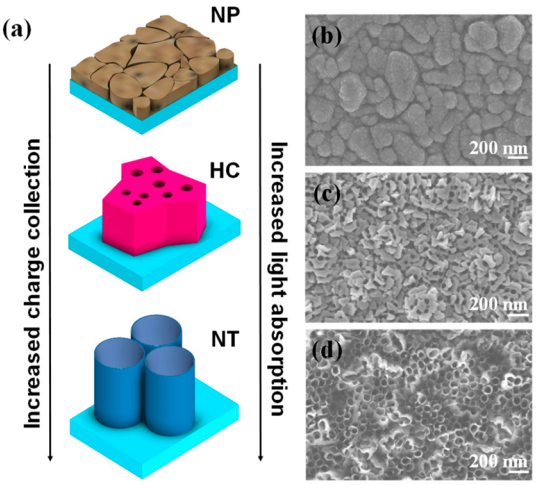

Figure 2. (a) Schematic of TiO_2 NP, HC, and NT microstructures; SEM of TiO_2 (b) NP, (c) HC, and (d) NT.

properties, incident-photon-to-current-efficiency (IPCE), STC, and internal-quantum-efficiency (IQE) provides unparalleled insight into the wavelength-dependent interplay of light trapping, sensitization and charge transport. In particular, using Br_3^-/Br^- and I_3^-/I^- as redox couples for the photoanode and the cathode, respectively, we show that TiO_2 nanotubes with ultrathin walls (<10 nm thick) exhibit the best photoelectrochemical performance (STC = 0.048%) thanks to optimal light trapping and charge collection. Remarkably, this corresponds to ∼50% increase compared to the thick-wall honeycomb structure, despite similar surface areas. Meanwhile, addition of plasmonic Au nanoparticles greatly increases the catalytic efficiency over the whole spectrum while providing extra light absorption and charge carriers in the visible range (sub-bandgap sensitization). Indeed, with Au nanoparticle decoration, the maximum IPCE increases from 47.4% to 54.7%, and IQE reaches 67% and STC increases by ∼25%. Overall, our Au/TiO_2 nanotube SPRC photoanode shows a high photocurrent of 0.098 mA/cm^2 and an excellent STC of 0.06%, comparable to recent state-of-the-art results (Table S1) despite the nonoptimized geometry of the testing cell[2]. Interestingly, this STC is among the best reported when compared to the corresponding theoretically STC (STC_{th}) value. These results highlight the importance of nanophotonic engineering of single, wide-bandgap SPRC photoelectrodes toward successfully addressing the trade-off between STC and cell-voltage.

EXPERIMENTAL SECTION

Sample Preparation. Both the TiO_2 nanotubes array and honeycomb structures were fabricated via electrochemical anodization in a two electrodes set up with Ti-coated fluorinated tin oxide (FTO) glass as the working electrode and Pt foil as the counter electrode.

https://doi.org/10.1021/acs.jpcc.2c05893
J. Phys. Chem. C 2023, 127, 11−21

Titanium thin films (1 μm) were deposited on FTO glass by using different magnetron sputtering techniques. For the HC microstructure, reactive Ti target (99.995%) was sputtered in RF mode under 400 W power supply. A mixture of argon (11 sccm) and oxygen (4 sccm) flow was injected into the sputtering chamber in order to directly grow the TiO_2 protecting film (80 nm) first. Subsequently, only the argon flow was used to grow the pure Ti layer (1 μm). For the NT sample, a normal Ti target (99.995%) was used in DC mode under 400 W power supply. After the desired thickness (1 μm) of Ti film was deposited on the entire FTO glass at 400 °C, a second layer of Ti (500 nm) was sputtered on half of the FTO at room temperature (Figure S1a). This additional Ti film was deposited to avoid metal etching at the electrode/electrolyte/air interface during the anodization process.

The Ti film was anodized in an ethylene glycol electrolyte containing 0.5 wt % NH_4F and 2.5 vol % deionized water under continuous stirring until the glass became transparent. For the nanotube growth, the single Ti layer part was totally immersed in electrolyte during anodization while the bilayer part was partly immersed. Hence, the electrolyte/air interface is positioned over the Ti bilayer, avoiding complete etching that would result in damages to the sample. The anodization was operated at 30 V while keeping the distance of these two electrodes at 20 mm. Figure S2 shows the current−time curves monitoring the conversion of Ti into TiO_2. After a peak current, the anodization current shows a flat plateau. Subsequently the anodization process must be stopped to avoid lift off. Both of these photoelectrodes are nearly fully anodized as the FTO glasses are transparent (Figure S1b). It is interesting that the reactive Ti has the higher current and needs less time than normal Ti for anodization.

Besides NT and HC microstructures, TiO_2 nanoparticles (NP) were also fabricated via directly sputtering TiO_2 on FTO using a reactive Ti target under a mixture of argon (11 sccm) and oxygen (4 sccm) flow.

The TiO_2 microstructures were then coated with thin Au films of defined thicknesses (2 nm) using the same sputtering device under room temperature (named NT/Au, HC/Au, and NP/Au). Next, all the samples (both the Au coated ones and the bare TiO_2 reference ones, named NT, HC, and NP) were annealed at 450 °C for 2 h with a heating rate of 2 °C/min to obtain highly crystallized and transparent TiO_2 electrodes. This thermal treatment can simultaneously accomplish crystallization of the amorphous TiO_2 into an anatase−rutile mixture phase and dewetting of the Au films into Au nanoparticles with small sizes.

Electrochemical Cell. The used H-cell consist of one catholyte chamber, one anolyte chamber, and a Nafion 115 separator in between. The photoanode with surface area of 0.25 cm^2 was inserted in the catholyte chamber, while the platinum foil was used as cathode in the anolyte chamber. KBr (1M)/LiH_2PO_4 (0.5 M) and KI (1 M)/I_2 (0.1 M)/LiH_2PO_4 (0.5 M) were chosen as catholyte and anolyte respectively, as they have superior reaction kinetics.[2] On the other hand, the redox potential of these two redox couples are between oxygen evolution reaction and hydrogen evolution reaction, which can suppress the side effects. The pH of the electrolyte is 4, which will be used for the conversion of the collected potentials (versus Ag/AgCl in 3 M KCl) to reversible hydrogen electrode (RHE) according to formula 1:

$$E(\mathrm{RHE}) = E(\mathrm{Ag/AgCl}) + 0.0591 \times \mathrm{pH} + E^0_{\mathrm{Ag/AgCl}}(0.205) \quad (1)$$

Material Characterization. The morphology and crystal structure of TiO_2 electrodes were characterized by a scanning electron microscope (Zeiss Gemini SEM 300) and X-ray diffractometer (XRD, Rigaku Synergy-I single crystal). X-ray photoelectron spectroscopy (XPS) analyses were performed using a PHI VersaProbe II scanning XPS microprobe (Physical Instruments AG, Germany) equipped with an Al Kα radiation source ($h\nu$ = 1486.6 eV).

Optical Measurement and Photoelectrochemical Test. A solar simulator (Newport 66984-300XF-R1 Xe lamp) with an AM 1.5 G filter was used as the light source. The photocurrent density as a function of time for different TiO_2 photoanodes was recorded via a potentiostat (Biologic, SP-300) by using a two electrodes H-cell (photoelectrode as the working electrode and Pt foil as the counter electrode) under 1 sun illumination (100 mW/cm^2) without bias. The power density of the incident light was calibrated to 1 sun by using an optical power meter (Thorlabs, PM100D) with thermal power sensor (Thorlabs, S350C). The UV−vis test was performed using a monochromator (Princeton Instruments, Acton SP2300) connected with an integrating sphere (Newport, 819D-IS-5.3). The optical density of monochromatic light was recorded by a detector (Newport, 818-UV/DB) as well as the hand-held laser power meter (Newport, 843-R-USB). The incident photon to current efficiency (IPCE) studies were performed using the monochromatic light with a 15 nm bandwidth, obtained with the same set up. In order to maximize the signal-to-noise ratio, the test was performed in a single-chamber three electrodes homemade cell (photoelectrode as the working electrode, Pt foil (Guangdong Carnd Energy Tec) as the counter electrode and leakage-free Ag/AgCl (Innovative Instruments, Inc.) as the reference electrode) with 1 M KBr/0.5 M LiH_2PO_4 electrolyte and under the application of 0.612 V.[57] The photocurrent signal with 20−20 s light on/off was recorded at each wavelength and normalized by the number of incident photon. This setup is also equipped with two cut wavelength filter. A long-pass filter cuts off photons with λ < 335 nm when measuring wavelength between 340 and 480 nm; another long-pass filter is used to cut off photons with λ < 495 nm during measurements in the 500−700 nm range. All samples were back-illuminated through the FTO glass with an illuminated area of 0.25 cm^2.

RESULTS AND DISCUSSION

TiO_2 is a wide bandgap semiconductor (3.2 eV) with good photocatalytic properties and a remarkable chemical stability as well as photocorrosion resistance, which made it a highly investigated substrate for photoelectrochemical applications.[58] Br_3^-/ Br^- redox couple with potential (1.09 V vs normal hydrogen electrode (NHE)), lower than the oxygen evolution reaction, and the I_3^-/I^- redox couple with potential at 0.54 V vs NHE, higher than the hydrogen evolution reaction, were used as the anolyte and catholyte respectively (Figure 1). Indeed, TiO_2 can easily drive these two redox couple reactions without external bias while avoiding water splitting. In order to study the synergistic effect of morphology and plasmonic engineering on TiO_2 performance as SPRC photoanode, we considered three distinct TiO_2 microstructures (Experimental

https://doi.org/10.1021/acs.jpcc.2c05893
J. Phys. Chem. C 2023, 127, 11−21

Table 1. Summary of Optical and Electrochemical Properties[a]

sample	active area $S\left(\frac{\text{mF}}{\text{cm}^2}\right)$	$\varepsilon_{cat} = \frac{\eta_{coll}}{\eta_{cat}} = \frac{S}{S_{NP}}$	Abs	$\varepsilon_{\text{Abs}} = \frac{\text{Abs}}{\text{Abs}_{NP}}$	$J_{ph}\left(\frac{\text{mA}}{\text{cm}^2}\right)$	$J_{ph,max}\left(\frac{\text{mA}}{\text{cm}^2}\right)$	$\eta_{coll}\eta_{cat} \sim \frac{J_{ph}}{J_{ph,\text{max}}}$	$\frac{J_{ph}}{J_{ph,max}\cdot S}$	$\varepsilon_{coll} = \frac{\eta_{coll}}{\eta_{coll,NP}}$	STC
NP	1.12	1.00	0.121	1.00	0.003	0.444	0.0068	0.0060	1.00	0.002
HC	2.80	**2.50**	0.165	**1.36**	0.052	0.601	0.0865	0.0309	**5.12**	**0.029**
NT	3.14	**2.80**	0.189	**1.56**	0.078	0.744	0.1048	0.0334	**5.53**	**0.048**
NT/Au	6.20	**5.54**	0.303	**2.50**	0.098	0.862	0.1137	0.0183	**3.04**	**0.06**

[a]It shows the impact of morphology and Au decoration on the electrochemically active surface area (S), which is proportional to the catalytic efficiency (η_{cat}), optical absorption (Abs), photocurrent density (J_{ph}), charge collection efficiency (η_{coll}), and solar-to-chemical (STC) efficiency.

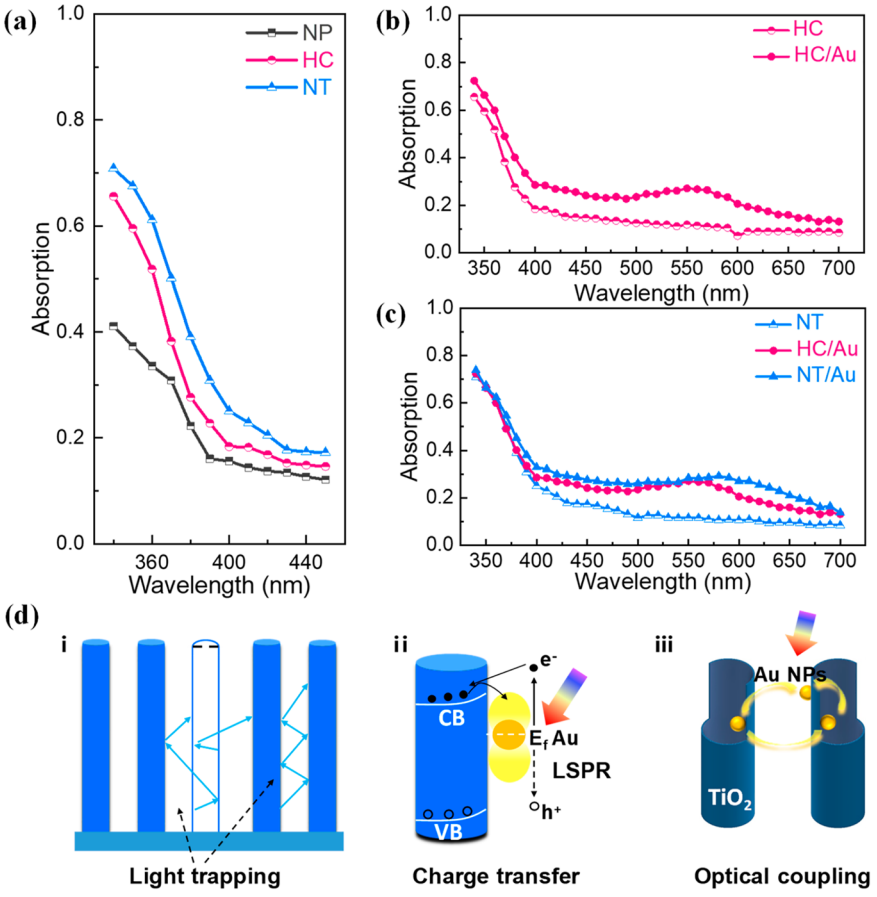

Figure 3. UV absorption spectrum of (a) different TiO_2 microstructures; UV−vis absorption spectrum of (b) HC, HC/Au and (c) NT, HC/Au and NT/Au; and (d) schematic of TiO_2 microstructure showing difference enhancement: (i) light trapping, (ii) LSPR and charge transfer, and (iii) optical coupling.

Section), which we call TiO_2 NP, TiO_2 HC and TiO_2 NT, as shown in Figure 2a.

Importantly, these microstructures are characterized by different active surface areas, electron transport distances, and light absorption that will deeply affect the reaction kinetics as well as the charge carrier generation/collection. NT and HC are obtained from different titanium films (normal and reactive, respectively, both with 1 μm thickness) via the same scalable anodization process. It can be seen from Figure S3a,d that the normal titanium film is smoother than the reactive titanium film before anodization. The larger uniform grains create more opportunities for the homogeneous growth of TiO_2 nanotubes, resulting in key morphological differences after anodization. Ordered NT, obtained from normal Ti, have a length of 1.2−1.5 μm (Figure S3f), a diameter of around 60−120 nm and an ultrathin wall of approximately 10 nm (Figure 2d). Figure S3f also shows that the initial titanium layer is fully anodized. This microstructure has a high surface area and is expected to exhibit effective charge carrier collection thanks to the short propagation distances involved. The HC microstructure (Figure 2c) is more compact than the NT. In particular, it exhibits thicker walls as well as fewer and narrower pores (diameter of 40−90 nm), resulting in longer charge carrier collection distances.[59] Finally, as a control sample, we deposited a compact TiO_2 film (also 1 μm thick) that is composed of large nanoparticles, resulting in the lowest electrolyte/electrode contact area and bulk-like charge generation/collection (Figure 2b). To get a quantitative comparison of the active surface area of these different photoelectrodes, cyclic voltammetry was used to measure the

https://doi.org/10.1021/acs.jpcc.2c05893
J. Phys. Chem. C 2023, 127, 11−21

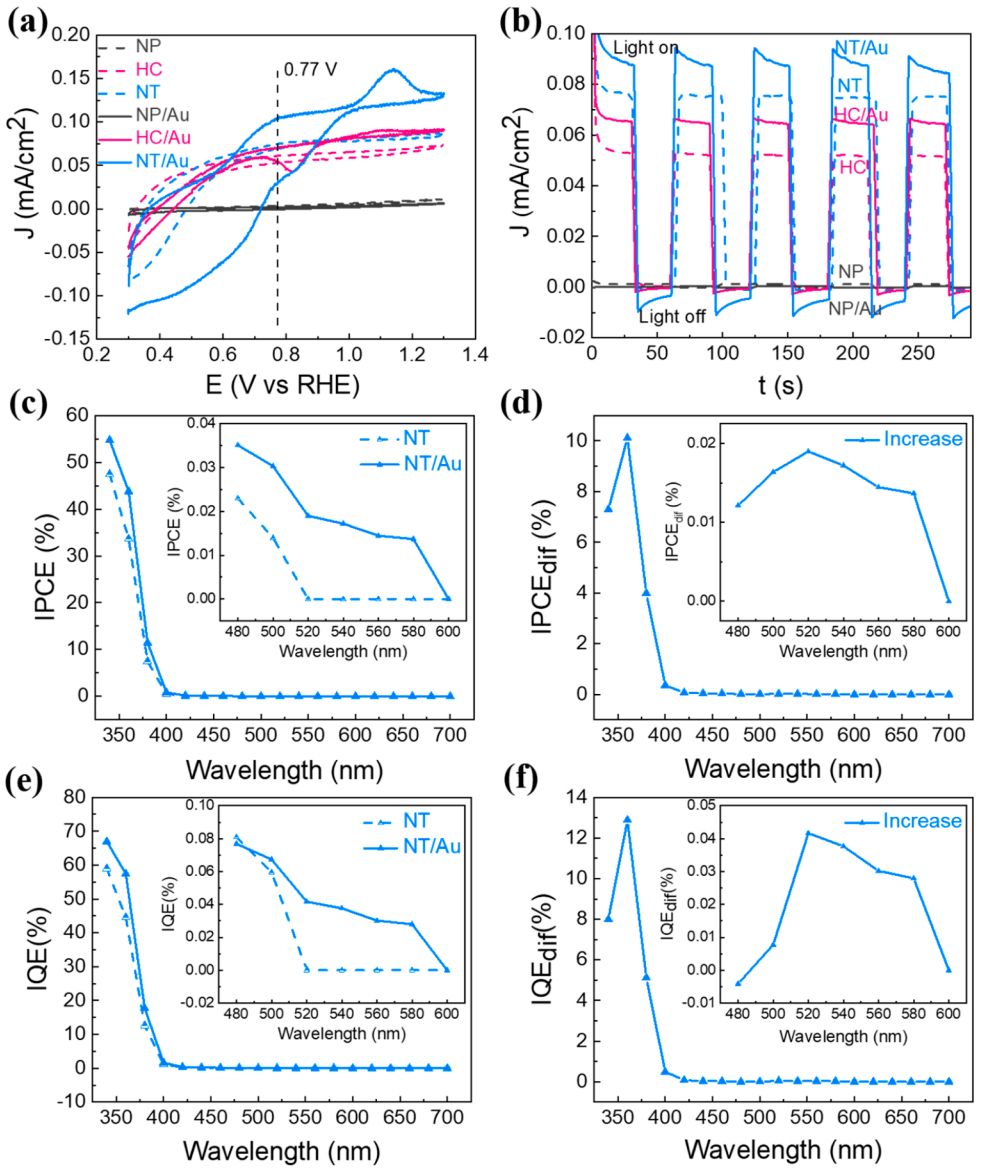

Figure 4. Cyclic voltammograms of (a) different photoelectrodes under AM 1.5G illumination was induced in 1 M KBr/0.5 M LiH_2PO_4 electrolyte; (b) photocurrent transient test of different microstructures (30−30 s light on−off) in H-cell; (c) IPCE spectra of NT and NT/Au under 0.612 V versus Ag/AgCl reference electrode; (d)) IPCE difference ($IPCE_{dif}$) between NT/Au and NT in UV−vis range and visible range (inset); (e) internal quantum efficiency (IQE) of NT/Au and NT; (f) IQE difference (IQE_{dif}) between NT/Au and NT in UV−vis range and visible range (inset).

electrochemical double-layer capacitances[60] (Figure S4). The electrochemically active surface area of NT, HC, and NP are 3.14 mF/cm^2, 2.8 mF/cm^2, and 1.12 mF/cm^2, respectively (Figure S4e). Hence, the active surface areas of NT and HC are similar (2.8 and 2.5 times higher than that of NP, respectively—Table 1). This allows us to assess separately the roles of surface area and charge collection. The XRD patterns of NT, HC and NP (Figure S5a) show that they all consist of both anatase and rutile phases.[61] The synergistic effect of the mixed-phase crystal structure and high specific surface area may help further improve photoelectrochemical performance.[62] Due to the FTO substrate, the peaks indexed at 26.5°, 33.7°, 51.6°, 61.6°, and 65.7° in all XRD patterns can be attributed to SnO_2. We finally note that HC and NT show more characteristic peaks ($A(101)$ and $A(200)$, at 25.27° and 48.01°, respectively) compared to NP, suggesting their better crystallization[63] thanks to a higher specific surface area (which allows a more complete annealing process) compared to dense NP.

All samples were subsequently decorated with plasmonic Au nanoparticles to assess their impact on optical and electronic processes. On one hand, electron−hole pairs generated in the metal can be injected into the adjacent n-type TiO_2 where they quickly relax to the conduction band edge and after moving to the cathode they become available to drive chemical reactions.[64,65] Thanks to proper band alignment, this process results in absorption and utilization of sub-bandgap photons. Meanwhile, electron transfer between TiO_2 and Au nanoparticles also induces a negative shift of the Fermi level of Au nanoparticles that can improve charge transfer at the TiO_2/electrolyte interface.[66] As shown in Figure S3, all TiO_2 morphologies are uniformly coated by Au nanoparticles. For

https://doi.org/10.1021/acs.jpcc.2c05893
J. Phys. Chem. C 2023, 127, 11−21

all three samples, the diameter of Au nanoparticles ranges from 5 to 20 nm, as estimated via ImageJ. NP/Au and HC/Au have an average diameter of 11 nm, while NT/Au have a larger fraction of small size nanoparticles with an average diameter of 9 nm (Figure S6). These result in larger contact area and more plasmonic sites. Indeed, the active surface area of the NT/Au sample is double that of the bare NTs (Table 1). As the average size of Au nanoparticles is much smaller than the diameter of the HC pores and NT, it is expected that both the top surface and the inner walls are coated by Au nanoparticles. The EDS results (Figure S7) show that NT/Au, HC/Au, and NP/Au all have a homogeneous Au decoration. It is worth noting that mapping of Au, Ti, and O $K\alpha_1$ for NT/Au shows more dark areas, associated with the bare tube space. This confirms that the anodization process is totally completed without any Ti residual. Also, this hollow tubular structure allows Au nanoparticles to deposit deeper inside the tubes, creating more plasmonic nanoparticles in the inner surface as Figure S8 shows. Figure S9 additionally depicts XPS spectra of Au(4f) for NT/Au and NT. The peaks of Au $4f_{7/2}$ and Au $4f_{5/2}$ are clearly shown at 84.05 and 87.8 eV for the sample which has been treated with Au sputtering. Finally, under slow scan mode, Au peaks (200)[67] at around 44.5° can be seen also in the XRD scans (Figure S5c), confirming a good combination of Au nanoparticles and TiO_2 microstructures.

The optical response of the bare TiO_2 microstructures was measured and compared with that of the Au coated samples. The total light absorption spectra, obtained from normal incidence transmission/reflection measurements in the UV−vis−NIR (340−700 nm) range, is shown in Figure S10a,b (see details in Experimental Section). Without Au coating, the UV absorption (340−425 nm) increases from NP to HC to NT (Figure 3a), integrated values being reported in Table 1. In particular, NT and HC exhibit a broadband antireflection effect (effective medium) as shown in Figure S10c,d while strongly enhancing light trapping (decreased transmission) (Figure 3d.i). All TiO_2/Au photoelectrodes (Figure 3b,c and Figure S10b) display enhanced visible light absorption (500−650 nm) due to the localized surface plasmon resonance (LSPR) effect[68] (Figure 3d.ii). In particular, for the NT sample, the LSPR peak is much broader (Figure 3c), with a maximum at ∼580 nm extending beyond 650 nm. This could be intuitively attributed to larger plasmonic nanoparticles. However, Au deposition conditions and interfacial properties are similar to those for the other two samples, which in fact exhibit comparable LSPR modes. We observe instead that the ultrathin walls of the nanotubes, whose thickness is comparable to the nanoparticle diameter, would allow optical coupling[69] between plasmonic nanoparticles deposited in adjacent nanotubes, as Figure 3d.iii shows. Also, there are more Au nanoparticles with smaller diameter coated on NT, resulting in smaller gap between them. This is indeed expected to result in a sizable red-shift and strengthening of the observed plasmonic resonances.[70]

Interestingly, Au nanoparticles increase the UV absorption of NP and HC samples, but they do not seem to affect the NT sample. Specifically, for NP, we observe that the addition of Au dramatically reduces reflection, likely due to preferential scattering of light into TiO_2 because of its high refractive index. For the HC sample, transmission is instead decreased thanks to enhanced light scattering and trapping. For the NT sample, however, optical effects are negligible, and any modification of the photoelectrochemical response in this wavelength range is expected to originate solely from electronic effects (i.e., improved charge transfer).

To investigate the reversibility and reaction kinetics of the photoelectrodes, cyclic voltammetry (CV) curves of as-prepared photoelectrodes were measured in a homemade three-electrode system under illumination and dark conditions with a sweeping rate of 20 mV/s. Figure 4a shows the CV scan of all photoelectrodes under illumination within 0.3−1.3 V versus RHE. We note that, in this potential range, oxygen and hydrogen evolution are not observed probably due to the overpotential (no bubbles on the electrode, standard reduction potentials of H_2O/O_2 is 1.23 V versus RHE and $2H^+/H_2$ is 0 V vs RHE). For the photoelectrodes without Au nanoparticles (dashed lines) the measured current density increases according to the estimated electrochemically active area. In particular, for NP the photocurrent density is very low (within 0.01 mA/cm^2) during the whole scanning range due to the small electrode/electrolyte interface and densely packed structure which impedes electrons and ions transport. On the other hand, all TiO_2/Au photoelectrodes (solid lines) except NP/Au exhibit an increased current density that is larger the higher the surface area. Most importantly, the shift-up in the potential of oxidation and reduction reaction for HC/Au and NT/Au, compared to the case without gold, indicate that the catalytic activity and the reversibility of these modified photoelectrodes are enhanced by the plasmonic nanoparticles, especially during the photocharging process. NT and NT/Au photoanodes, which exhibit the best performance, were also scanned within a broader range, 0.1−1.7 V versus RHE, both under dark and illumination (Figure S11c). We observe that there is nearly no current for NT in dark conditions up to 1.4 V. Instead, even in dark, NT/Au shows current already at 1.0 V with a steep increase after 1.4 V. This may due to Au nanoparticles driving the redox couple under a lower bias of 1.0 V while accelerating water splitting after 1.4 V versus RHE. In fact, bubbles were observed on the photoanode side in the latter case. Under illumination, we observe a clear shift to lower potential for oxidation and reduction states that, combined with the higher currents, confirms enhanced reactivity with the redox couple reaction of KBr and holes from photoelectrode surface. NT/Au photoanode has also been scanned for three cycles under dark and illumination in Figure S11a and S11b, respectively, confirming its reaction stability and chemical resistance under bias.

A photocurrent density−time (J−t) measurement under solar irradiation (see Experimental Section) has been performed for all samples using an H-cell without external voltage bias, driving bromine ion oxidation on the photoanode and iodine ion reduction on the cathode. The solar energy conversion and storage of this solar powered redox cell depends on the different TiO_2 microstructures as well as the plasmonic effect. Figure 4b shows the photoresponse behavior of the considered photoanodes while Figure S11d shows their photocurrent stability for long operation time (1 h). A stable pulse signal with instantaneous photoresponse could be obtained under this periodic test for all TiO_2 photoanodes, indicating their excellent photoactivity. As the reaction continues, the colorless KBr solution gradually turned yellow, confirming that the nonspontaneous oxidation reaction ($2Br^- + 2h^+ \leftrightarrow Br_2$) took place. As shown in Figure 4b, the NT photocurrent density is large and equal to 0.078 mA/cm^2. This can be attributed to the unique combination of strong light absorption and effective charge carrier collection, the latter

https://doi.org/10.1021/acs.jpcc.2c05893
J. Phys. Chem. C 2023, 127, 11−21

likely due to the comparable charge carrier mean free path and nanotube wall thickness. The NT/Au sample exhibits the largest photocurrent density at 0.098 mA/cm^2, i.e., a 25% improvement. Importantly, we recall that, in the UV range of the spectrum, Au nanoparticles did not contribute to any further light absorption. Instead, they enhance light absorption in the visible range, due to LSPR excitation, and are expected to improve interfacial charge transfer across the whole spectrum, due to higher electrochemically active surface area as shown in Figure S4e. We note that, with the chosen anolyte (I_3^-/I^- redox couple −0.54 V versus NHE, 0.77 V versus RHE), the NT/Au photoanode was expected to have the highest photocurrent density at around 0.11 mA/cm^2 as shown in Figure 4a. The decrease compared to the cyclic voltammetry test can be attributed to the concentration polarization and poor mass transport near electrode surface in the large H-cell chamber without stirring, as well as the resistance of Nafion membrane used for ion transport.[2] With prolonged irradiation time, Figure S11d showed that the photocurrent density for both NT and NT/Au did not decrease and the photocurrent density retention is higher than 95%. These results once again confirm the stability of the TiO_2 nanotubes. The HC photoanode exhibits a photocurrent density of 0.052 mA/cm^2. At longer times, however, this value decreases to 0.042 mA/cm^2, indicating a retention of only 81%. With Au decoration, a ∼28% improvement of photocurrent density is observed (0.067 mA/cm^2) together with an increased retention (90%). This indicates that the plasmonic design can simultaneously improve photoelectrochemical performance and sample stability. Yet, we observe that HC/Au photoanode has ∼33% lower photocurrent density compared to NT/Au, despite equal UV absorption, comparable visible absorption as well as similar electrochemically active surfaces. Thus, a decrease in charge collection is expected to be responsible for this difference. Last, we note that the photocurrent density of NP is only 0.003 mA/cm^2 owing to its densely compact structure with poor electron diffusion kinetics and low surface area. Interestingly, NP/Au has an even lower photocurrent density of 0.001 mA/cm^2 despite increased visible absorption. Indeed, if the generated electron−hole pairs are not sufficient compared to the amount of Au nanoparticles, these will no longer act as an intermediate for charge transport but rather decrease the TiO_2 electrode/electrolyte interface, blocking the transfer path and causing a photocurrent decrease. Thus, Au decoration creating plasmonic structure should work synergistically with the microstructure. Therefore, it is necessary to optimize both the optical effects (better light absorption) and the electronic effects (smaller electron transport path, enough active interface for reaction) to get a superior photoelectrochemical performance.

Based on the available data, it is possible to perform a quantitative analysis of the role of morphology and Au decoration on the optical and electrochemical behavior of the photoanodes. In particular, we can express the measured photocurrent density as

$$J_{ph} = \int_{\lambda_i}^{\lambda_e} \mathrm{Abs}(\lambda)\Phi(\lambda)\,\mathrm{d}\lambda \cdot \eta_{coll} \cdot \eta_{cat} \tag{2}$$

where $\mathrm{Abs}(\lambda) = 1 - T(\lambda) - R(\lambda)$ is the portion of photons being absorbed, $\Phi(\lambda)\,\mathrm{d}\lambda$ is the photon flux defined by AM 1.5G spectrum. Integration is performed in the wavelength range [340−675 nm], defined by the characteristics of our spectrometer. This is nonetheless a good approximation of the integral over the full solar spectrum. In fact, at shorter wavelengths, the photon flux is very low ($\Phi_{\lambda<340\mathrm{nm}} \approx 0$) while absorption becomes negligible at longer wavelengths ($\mathrm{Abs}_{\lambda>675\ \mathrm{nm}} \rightarrow 0$). Additionally, η_{coll} is the charge separation/collection efficiency in the semiconductor and η_{cat} is the catalytic efficiency. The latter is related to the efficiency of charge transfer at the solid/liquid interface.

Determining a priori these efficiencies is challenging because the morphology simultaneously affects the number of active sites as well as the charge collection. In addition, the mass transport, over potential, reaction kinetics, resistance and other parameters all affect our experimental photocurrent. However, previous literature[60] suggests that the active surface area, S, is proportional to the catalytic efficiency, i.e. $\eta_{cat} \sim S$. We also observe that for an ideal case with perfect charge transfer, the maximum photocurrent depends solely on light absorption:

$$J_{ph,\max} = \int_{\lambda_i}^{\lambda_e} \mathrm{Abs}(\lambda)\Phi(\lambda)\,\mathrm{d}\lambda \tag{3}$$

Therefore, the collection efficiency can be estimated as

$$\eta_{coll} \propto \frac{J_{ph}}{J_{ph,\max} \cdot S} \tag{4}$$

As shown in Table 1, this value increases from NP, to HC to NT. Additionally, using the NP sample as a reference, we can recast eq 2 as

$$\begin{aligned} J_{ph} &= J_{ph,\max} \cdot (\eta_{coll}\eta_{cat})_{NP} \frac{\eta_{coll}}{\eta_{coll,NP}} \frac{\eta_{cat}}{\eta_{cat,NP}} \\ &= J_{ph,\max} \cdot (\eta_{coll} \cdot S)_{NP} \varepsilon_{coll} \varepsilon_{cat} \end{aligned} \tag{5}$$

where $\varepsilon_{coll} = \frac{\eta_{coll}}{\eta_{coll,NP}}$ and $\varepsilon_{cat} = \frac{S}{S_{NP}}$. This then allow us to quantify the increase in collection efficiency with respect to the NP morphology:

$$\varepsilon_{coll} = \frac{J_{ph}}{J_{ph,\max} \cdot (\eta_{coll}\eta_{cat})_{NP} \varepsilon_{cat}} \tag{6}$$

Overall, Abs, ε_{cat}, and ε_{coll} provide quantitative information about the light harnessing, catalytic, and charge separation/collection properties of each sample. Table 1 summarizes the performance of the three morphologies and, for our best sample (NT/Au), also the role of the Au nanoparticles. We observe that the morphology has the largest impact on the charge collection efficiency (ε_{coll}) likely due to the reduction in propagation distance. Instead, Au decoration has the largest impact on the catalytic efficiency. However, it reduces the charge collection efficiency compared to the bare morphology (NT), possibly because of an increased charge recombination at the metal/semiconductor interface due to the concurrent charge carrier generation in the metal.[71] Nonetheless, for NT/Au, the largely improved catalytic efficiency together with the increase in absorption largely compensate the reduction in collection efficiency, overall resulting in an improved performance of the device. Yet, if these contributions are insufficient, a decrease in performance could occur, as observed for the case of NP/Au samples. Thus, morphology and plasmonic decoration must be concurrently optimized in order to have a net benefit.

https://doi.org/10.1021/acs.jpcc.2c05893
J. Phys. Chem. C 2023, 127, 11−21

Knowing the maximum output photocurrent density without bias, J_{ph}, the overall STC efficiency can be also calculated as[13]

$$STC = \frac{J_{ph} \cdot E_{ocv}}{P_{in}} \cdot 100 \quad (7)$$

where E_{ocv} is the potential difference between two redox couples and P_{in} is the incident power density. As Br_3^-/Br^- and I_3^-/I^- are used, the obtained STC for NT/Au photoanode in the H-cell is around 0.06%. The maximum theoretical photocurrent density of TiO_2 can be calculated from eq 3 using literature optical transmission and reflection data[48] and integrating from the onset of the solar spectrum (λ_i = 280 nm) to the semiconductor bandgap ($\lambda_e = \lambda_g$). After assuming 100% quantum efficiency for photons with energy above bandgap, and considering the dark saturation current density, we can get the photocurrent density as a function of the semiconductor bandgap.[21] Thus, the maximum ideal STC efficiency for TiO_2 photoelectrode using the same redox couples with potential difference at 0.55 V is 0.6% at a maximum photocurrent density around 1.05 mA/cm^2 (without considering mass transport, state of charge, overpotential and cell resistance). Considering what plasmonic structures can do to remarkably improve the performance of TiO_2 NT, it is expected to see how much this plasmonic strategy can further enhance the maximum solar to chemical reaction of different photoelectrodes with even better performing redox couples.

While these numbers provide an integral view of the device behavior, we can gain further insight from the spectrally resolved response of the photoanodes. We thus measured the incident photon to current efficiency of NT and NT/Au samples using 1 M KBr and 0.5 M LiH_2PO_4 buffer solution is shown in Figure 4c. The IPCE was obtained under 0.612 V versus Ag/AgCl reference electrode, i.e., near the Br^- oxidation potential,[72,73] and under monochromatic illumination with a 20 nm λ step-size across the 340−680 nm range. The spectra were calculated by measuring the photocurrent transient (20−20s light on−off under 5 cycles) under monochromatic light as Figure S12 shows. The NT/Au sample has a maximum IPCE 54.7% at 350 nm, which is significantly higher than NT with its IPCE of 47.4%. Recalling that UV light absorption (340−400 nm) is similar for these two photoanodes (Figure 3c), we conclude that, in this spectral range, the improvement is related to the higher catalytic efficiency ascribed to the Au nanoparticles, which favor electron transfer to the redox-molecules from the bulk semiconductor. The inset in Figure 4c shows the IPCE in the visible region. After 550 nm, NT/Au still shows a clear photo response while the photocurrent of NT decreases to zero around 500 nm. The IPCE difference ($IPCE_{dif}$) between these two photoanodes as a function of wavelength (Figure 4d) closely follows the line shape of the corresponding optical absorption spectrum (peak around 520 nm). This confirms the unique contribution from plasmonic sensitization in extending the functionality of the photoanode to sub-bandgap wavelengths, an effect that could not be obtained solely with microstructure engineering. Finally, to gain deeper insight into the performance of NT/Au, internal quantum efficiency (IQE) was also computed (Figure 4e,f), focusing on the absorbed photons only. NT/Au shows a maximum IQE of 67%, significantly larger than that for NT (59%), indicating that NT/Au has a better inherent performance thanks to the synergistic combination of microstructure (charge collection) and plasmonic design (higher catalytic efficiency as shown in Table 1). Hence this proves that plasmonic Au nanoparticles can overall promote photogenerated electron harnessing.

CONCLUSIONS

In summary, we studied the synergistic effect of plasmonic/nanophotonic engineering and micro-/nanostructuring in wide-bandgap SPRCs photoelectrodes. Using three morphologies of Au-decorated TiO_2 photoanodes, namely nanotubes, honeycombs, and nanoparticles, and a complete optical and photoelectrochemical characterization, we showed the critical wavelength-dependent interplay between light trapping, surface area, charge collection, and recombination as well as sub-bandgap plasmonic sensitization. In particular, we showed that while microstructures generally improve light trapping and hence absorption, nm-scale details of these features play a critical role in charge collection (i.e., thin-walled nanotubes have 50% higher STC compared to thick-walled honeycombs). Furthermore, we identified the spectrally distinct roles of plasmonic nanoparticles. Despite a negative impact on the collection efficiency, likely due to enhanced recombination, these simultaneously contribute to enhanced light absorption, improved interfacial charge carrier transfer as well as photogenerated charge carriers at sub-bandgap photon energies. When acting synergistically with the morphology, which can strongly improve the collection efficiency, these lead to an overall increase of the device performance. Indeed, Au-sensitized TiO_2 nanotubes results a 25% increase of STC compared to bare ones. Overall, they exhibit the highest photocurrent (0.098 mA/cm^2), and an STC of 0.06% which is on-par with state-of-the-art results and among the best in comparison to ideal STC values.

Further improvement of the SPRCs system can be approached by a carefully engineered microfluidic SPRC reactor with low parasitic losses and optimized mass transport. Furthermore, we envision that combining this approach with the use of nonaqueous,[74] high potential redox cells would allow the full exploitation of the advantages of TiO_2 as a highly stable, wide bandgap material for SPRCs. More broadly, it will be possible to improve the photoelectrochemical performance of semiconductors with intrinsically poor charge transport (i.e., Fe_2O_3) or light absorption, by synergistically combining nanophotonic and microstructure engineering based on the dielectric properties of the identified materials for the photoelectrode used in SPRCs devices. Indeed, careful design of large surface area, ultrathin metasurfaces can boost above bandgap light harnessing while minimizing charge recombination.[75] In fact, these losses can be greatly reduced if the semiconductor size becomes comparable to the charge carrier mean free path, as we showed from NP to HC and NT. Concurrently, a broad palette of plasmonic materials, such as Au, Ag, Cu, Al, or TiN, can be used, either individually or in multimetallic combinations, to arbitrarily tailor the optical response, the sensitization characteristics, and the electrochemical properties of the photoelectrodes. Finally, we envision that engineering of complementary photothermal effects could also help in controlling the local activity and kinetics of redox reactions. Overall, these results aim at triggering broader use of careful nanophotonic engineering for both light and charge carrier management in rechargeable solar energy storage devices toward simple and high discharge voltage systems with maximized performance.

https://doi.org/10.1021/acs.jpcc.2c05893
J. Phys. Chem. C 2023, 127, 11−21

■ ASSOCIATED CONTENT

Supporting Information

The Supporting Information is available free of charge at https://pubs.acs.org/doi/10.1021/acs.jpcc.2c05893.

Additional information about reported state-of-the-art TiO_2-based solar powered redox cells; schematic of Ti film anodization; EDS, XRD, XPS, and CV characterization results of the TiO_2 photoanodes; TiO_2 photoanodes stability test; data acquisitions for relative active surface area and Au nanoparticles size; UV−vis absorption spectrum of TiO_2 microstructures; and IPCE and IQE for TiO_2 nanotubes-based samples (PDF)

■ AUTHOR INFORMATION

Corresponding Author

Giulia Tagliabue − *Laboratory of Nanoscience for Energy Technologies (LNET), STI, École Polytechnique Fédérale de Lausanne, 1015 Lausanne, Switzerland;* orcid.org/0000-0003-4587-728X; Email: giulia.tagliabue@epfl.ch

Authors

Jiaming Ma − *Laboratory of Nanoscience for Energy Technologies (LNET), STI, École Polytechnique Fédérale de Lausanne, 1015 Lausanne, Switzerland;* orcid.org/0000-0003-4311-0640

Kiseok Oh − *Laboratory of Nanoscience for Energy Technologies (LNET), STI, École Polytechnique Fédérale de Lausanne, 1015 Lausanne, Switzerland*

Complete contact information is available at: https://pubs.acs.org/10.1021/acs.jpcc.2c05893

Notes

The authors declare no competing financial interest.

■ ACKNOWLEDGMENTS

The authors acknowledge the support of the Swiss National Science Foundation (Eccellenza Grant #194181). J.M. acknowledges the support of the China Scholarship Council (201906210091). The authors also acknowledge the support of the following experimental facilities at EPFL: Interdisciplinary Centre for Electron Microscopy (CIME) and Center of MicroNano Technology (CMI). Finally, the authors would like to thank Mr. Nathanaël Restori for help with the solar simulator set up.

■ REFERENCES

(1) Cao, L.; Skyllas-Kazacos, M.; Wang, D.-W. Solar Redox Flow Batteries: Mechanism, Design, and Measurement. *Adv. Sustain. Syst* **2018**, *2* (8−9), 1800031.

(2) Zhou, Y.; Zhang, S.; Ding, Y.; Zhang, L.; Zhang, C.; Zhang, X.; Zhao, Y.; Yu, G. Efficient Solar Energy Harvesting and Storage through a Robust Photocatalyst Driving Reversible Redox Reactions. *Adv. Mater.* **2018**, *30* (31), 1802294.

(3) Azevedo, J.; Seipp, T.; Burfeind, J.; Sousa, C.; Bentien, A.; Araújo, J. P.; Mendes, A. Unbiased Solar Energy Storage: Photoelectrochemical Redox Flow Battery. *Nano Energy* **2016**, *22*, 396−405.

(4) Weber, A. Z.; Mench, M. M.; Meyers, J. P.; Ross, P. N.; Gostick, J. T.; Liu, Q. Redox Flow Batteries: A Review. *J. Appl. Electrochem.* **2011**, *41* (10), 1137.

(5) Zeng, Q.; Lai, Y.; Jiang, L.; Liu, F.; Hao, X.; Wang, L.; Green, M. A. Integrated Photorechargeable Energy Storage System: Next-Generation Power Source Driving the Future. *Adv. Energy Mater.* **2020**, *10* (14), 1903930.

(6) Li, W.; Jin, S. Design Principles and Developments of Integrated Solar Flow Batteries. *Acc. Chem. Res.* **2020**, *53* (11), 2611−2621.

(7) Memming, R. In Solid-Liquid Interface. *Semiconductor Electrochemistry*; John Wiley: 2000; Vol.3, pp 81−111.

(8) Gentil, S.; Reynard, D.; Girault, H. H. Aqueous Organic and Redox-Mediated Redox Flow Batteries: A Review. *Curr. Opin. Electrochem* **2020**, *21*, 7−13.

(9) Soloveichik, G. L. Flow Batteries: Current Status and Trends. *Chem. Rev.* **2015**, *115* (20), 11533−11558.

(10) Gong, K.; Fang, Q.; Gu, S.; Li, S. F. Y.; Yan, Y. Nonaqueous Redox-Flow Batteries: Organic Solvents, Supporting Electrolytes, and Redox Pairs. *Energy Environ. Sci.* **2015**, *8* (12), 3515−3530.

(11) Liao, S.; Zong, X.; Seger, B.; Pedersen, T.; Yao, T.; Ding, C.; Shi, J.; Chen, J.; Li, C. Integrating a Dual-Silicon Photoelectrochemical Cell into a Redox Flow Battery for Unassisted Photocharging. *Nat. Commun.* **2016**, *7* (1), 11474.

(12) Fu, H.-C.; Li, W.; Yang, Y.; Lin, C.-H.; Veyssal, A.; He, J.-H.; Jin, S. An Efficient and Stable Solar Flow Battery Enabled by a Single-Junction GaAs Photoelectrode. *Nat. Commun.* **2021**, *12* (1), 156.

(13) Cheng, Q.; Fan, W.; He, Y.; Ma, P.; Vanka, S.; Fan, S.; Mi, Z.; Wang, D. Photorechargeable High Voltage Redox Battery Enabled by Ta_3N_5 and GaN/Si Dual-Photoelectrode. *Adv. Mater.* **2017**, *29* (26), 1700312.

(14) McKone, J. R.; DiSalvo, F. J.; Abruña, H. D. Solar Energy Conversion, Storage, and Release Using an Integrated Solar-Driven Redox Flow Battery. *J. Mater. Chem. A* **2017**, *5* (11), 5362−5372.

(15) Shi, B.; Qi, Y.; Tian, L. Fabrication of Ag_2S Quantum Dots Sensitized CdSe Photoelectrodes and Its Photoelectric Performance. *Mater. Chem. Phys.* **2020**, *240*, 122177.

(16) Sun, J.; Xia, W.; Zheng, Q.; Zeng, X.; Liu, W.; Liu, G.; Wang, P. Increased Active Sites on Irregular Morphological α-Fe_2O_3 Nanorods for Enhanced Photoelectrochemical Performance. *ACS Omega* **2020**, *5* (21), 12339−12345.

(17) Wedege, K.; Azevedo, J.; Khataee, A.; Bentien, A.; Mendes, A. Direct Solar Charging of an Organic−Inorganic, Stable, and Aqueous Alkaline Redox Flow Battery with a Hematite Photoanode. *Angew. Chem. Int. Ed* **2016**, *55* (25), 7142−7147.

(18) Wang, L.; Schmid, M.; Nilsson, Z. N.; Tahir, M.; Chen, H.; Sambur, J. B. Laser Annealing Improves the Photoelectrochemical Activity of Ultrathin $MoSe_2$ Photoelectrodes. *ACS Appl. Mater. Interfaces* **2019**, *11* (21), 19207−19217.

(19) Wedege, K.; Bae, D.; Smith, W. A.; Mendes, A.; Bentien, A. Solar Redox Flow Batteries with Organic Redox Couples in Aqueous Electrolytes: A Minireview. *J. Phys. Chem. C* **2018**, *122* (45), 25729−25740.

(20) Zhang, S.; Chen, C.; Zhou, Y.; Qian, Y.; Ye, J.; Xiong, S.; Zhao, Y.; Zhang, X. TiO_2-Photoanode-Assisted Direct-Solar-Energy Harvesting and Storage in a Solar-Powered Redox Cell Using Halides as Active Materials. *ACS Appl. Mater. Interfaces* **2018**, *10* (27), 23048−23054.

(21) Bae, D.; Faasse, G. M.; Kanellos, G.; Smith, W. A. Unravelling the Practical Solar Charging Performance Limits of Redox Flow Batteries Based on a Single Photon Device System. *Sustain. Energy Fuels* **2019**, *3* (9), 2399−2408.

(22) Tian, G.; Jervis, R.; Briscoe, J.; Titirici, M.; Sobrido, A. J. Efficient Harvesting and Storage of Solar Energy of an All-Vanadium Solar Redox Flow Battery with a MoS_2@TiO_2 Photoelectrode. *J. Mater. Chem. A* **2022**, *10* (19), 10484−10492.

(23) da Silva Lopes, T.; Dias, P.; Monteiro, R.; Vilanova, A.; Ivanou, D.; Mendes, A. A 25 cm^2 Solar Redox Flow Cell: Facing the Engineering Challenges of Upscaling. *Adv. Energy Mater.* **2022**, *12* (5), 2102893.

(24) Li, W.; Fu, H.-C.; Zhao, Y.; He, J.-H.; Jin, S. 14.1% Efficient Monolithically Integrated Solar Flow Battery. *Chem.* **2018**, *4* (11), 2644−2657.

(25) Li, W.; Fu, H.-C.; Li, L.; Cabán-Acevedo, M.; He, J.-H.; Jin, S. Integrated Photoelectrochemical Solar Energy Conversion and

Organic Redox Flow Battery Devices. *Angew. Chem. Int. Ed* **2016**, *55* (42), 13104−13108.
(26) Warren, S. C.; Thimsen, E. Plasmonic Solar Water Splitting. *Energy Environ. Sci.* **2012**, *5* (1), 5133−5146.
(27) Murdoch, M.; Waterhouse, G. I. N.; Nadeem, M. A.; Metson, J. B.; Keane, M. A.; Howe, R. F.; Llorca, J.; Idriss, H. The Effect of Gold Loading and Particle Size on Photocatalytic Hydrogen Production from Ethanol over Au/TiO_2 Nanoparticles. *Nat. Chem.* **2011**, *3* (6), 489−492.
(28) Thimsen, E.; Le Formal, F.; Grätzel, M.; Warren, S. C. Influence of Plasmonic Au Nanoparticles on the Photoactivity of Fe_2O_3 Electrodes for Water Splitting. *Nano Lett.* **2011**, *11* (1), 35−43.
(29) Ghobadi, T. G. U.; Ghobadi, A.; Ozbay, E.; Karadas, F. Strategies for Plasmonic Hot-Electron-Driven Photoelectrochemical Water Splitting. *ChemPhotoChem.* **2018**, *2* (3), 161−182.
(30) Ghobadi, T. G. U.; Ghobadi, A.; Soydan, M. C.; Vishlaghi, M. B.; Kaya, S.; Karadas, F.; Ozbay, E. Strong Light−Matter Interactions in Au Plasmonic Nanoantennas Coupled with Prussian Blue Catalyst on $BiVO_4$ for Photoelectrochemical Water Splitting. *ChemSusChem* **2020**, *13* (10), 2577−2588.
(31) Mo, J.; Barbosa, E. C. M.; Wu, S.; Li, Y.; Sun, Y.; Xiang, W.; Li, T.; Pu, S.; Robertson, A.; Wu, T.; et al. Atomic-Precision Tailoring of Au−Ag Core−Shell Composite Nanoparticles for Direct Electrochemical-Plasmonic Hydrogen Evolution in Water Splitting. *Adv. Funct. Mater.* **2021**, *31* (30), 2102517.
(32) Song, K.; Lee, H.; Lee, M.; Park, J. Y. Plasmonic Hot Hole-Driven Water Splitting on Au Nanoprisms/P-Type GaN. *ACS Energy Lett.* **2021**, *6* (4), 1333−1339.
(33) Yu, M.-J.; Chang, C.-L.; Lan, H.-Y.; Chiao, Z.-Y.; Chen, Y.-C.; Howard Lee, H. W.; Chang, Y.-C.; Chang, S.-W.; Tanaka, T.; Tung, V.; et al. Plasmon-Enhanced Solar-Driven Hydrogen Evolution Using Titanium Nitride Metasurface Broadband Absorbers. *ACS Photonics* **2021**, *8* (11), 3125−3132.
(34) Zhang, D.; Wang, M.; Brolo, A. G.; Shen, J.; Li, X.; Huang, S. Enhanced Performance of Dye-Sensitized Solar Cells Using Gold Nanoparticles Modified Fluorine Tin Oxide Electrodes. *J. Phys. Appl. Phys.* **2013**, *46* (2), 024005.
(35) Li, Y.; Wang, H.; Feng, Q.; Zhou, G.; Wang, Z.-S. Gold Nanoparticles Inlaid TiO_2 Photoanodes: A Superior Candidate for High-Efficiency Dye -Sensitized Solar Cells. *Energy Environ. Sci.* **2013**, *6* (7), 2156−2165.
(36) Choudhury, B. D.; Lin, C.; Shawon, S. M. A. Z.; Soliz-Martinez, J.; Huq, H.; Uddin, M. J. A Photoanode with Hierarchical Nanoforest TiO_2 Structure and Silver Plasmonic Nanoparticles for Flexible Dye Sensitized Solar Cell. *Sci. Rep* **2021**, *11* (1), 7552.
(37) Javed, H. M. A.; Sarfaraz, M.; Nisar, M. Z.; Qureshi, A. A.; e Alam, M. F.; Que, W.; Yin, X.; Abd-Rabboh, H. S. M.; Shahid, A.; Ahmad, M. I.; et al. Plasmonic Dye-Sensitized Solar Cells: Fundamentals, Recent Developments, and Future Perspectives. *ChemistrySelect* **2021**, *6* (34), 9337−9350.
(38) DuChene, J. S.; Tagliabue, G.; Welch, A. J.; Cheng, W.-H.; Atwater, H. A. Hot Hole Collection and Photoelectrochemical CO_2 Reduction with Plasmonic Au/p-GaN Photocathodes. *Nano Lett.* **2018**, *18* (4), 2545−2550.
(39) Li, Y.; Wen, M.; Wang, Y.; Tian, G.; Wang, C.; Zhao, J. Plasmonic Hot Electrons from Oxygen Vacancies for Infrared Light-Driven Catalytic CO_2 Reduction on Bi_2O_{3-x}. *Angew. Chem.* **2021**, *133* (2), 923−929.
(40) Vu, N.-N.; Kaliaguine, S.; Do, T.-O. Plasmonic Photocatalysts for Sunlight-Driven Reduction of CO_2: Details, Developments, and Perspectives. *ChemSusChem* **2020**, *13* (16), 3967−3991.
(41) Devasia, D.; Wilson, A. J.; Heo, J.; Mohan, V.; Jain, P. K. A Rich Catalog of C−C Bonded Species Formed in CO_2 Reduction on a Plasmonic Photocatalyst. *Nat. Commun.* **2021**, *12* (1), 2612.
(42) Collado, L.; Reynal, A.; Fresno, F.; Barawi, M.; Escudero, C.; Perez-Dieste, V.; Coronado, J. M.; Serrano, D. P.; Durrant, J. R.; de la Peña O'Shea, V. A. Unravelling the Effect of Charge Dynamics at the Plasmonic Metal/Semiconductor Interface for CO_2 Photoreduction. *Nat. Commun.* **2018**, *9* (1), 4986.
(43) Lu, X.; Rycenga, M.; Skrabalak, S. E.; Wiley, B.; Xia, Y. Chemical Synthesis of Novel Plasmonic Nanoparticles. *Annu. Rev. Phys. Chem.* **2009**, *60* (1), 167−192.
(44) Kochuveedu, S. T.; Jang, Y. H.; Kim, D. H. A Study on the Mechanism for the Interaction of Light with Noble Metal-Metal Oxide Semiconductor Nanostructures for Various Photophysical Applications. *Chem. Soc. Rev.* **2013**, *42* (21), 8467−8493.
(45) Liu, M.; Pang, Y.; Zhang, B.; De Luna, P.; Voznyy, O.; Xu, J.; Zheng, X.; Dinh, C. T.; Fan, F.; Cao, C.; et al. Enhanced Electrocatalytic CO_2 Reduction via Field-Induced Reagent Concentration. *Nature* **2016**, *537* (7620), 382−386.
(46) Kamarudheen, R.; Aalbers, G. J. W.; Hamans, R. F.; Kamp, L. P. J.; Baldi, A. Distinguishing Among All Possible Activation Mechanisms of a Plasmon-Driven Chemical Reaction. *ACS Energy Lett.* **2020**, *5* (8), 2605−2613.
(47) Zhang, X.; Chen, Y. L.; Liu, R.-S.; Tsai, D. P. Plasmonic Photocatalysis. *Rep. Prog. Phys.* **2013**, *76* (4), 046401.
(48) Anderson, A. Y.; Bouhadana, Y.; Barad, H.-N.; Kupfer, B.; Rosh-Hodesh, E.; Aviv, H.; Tischler, Y. R.; Rühle, S.; Zaban, A. Quantum Efficiency and Bandgap Analysis for Combinatorial Photovoltaics: Sorting Activity of Cu−O Compounds in All-Oxide Device Libraries. *ACS Comb. Sci.* **2014**, *16* (2), 53−65.
(49) Chang, C.-Y.; Yamakata, A.; Tseng, W. J. Effect of Surface Plasmon Resonance and the Heterojunction on Photoelectrochemical Activity of Metal-Loaded TiO_2 Electrodes under Visible Light Irradiation. *J. Phys. Chem. C* **2022**, *126* (30), 12450−12459.
(50) Tagliabue, G.; DuChene, J. S.; Abdellah, M.; Habib, A.; Gosztola, D. J.; Hattori, Y.; Cheng, W.-H.; Zheng, K.; Canton, S. E.; Sundararaman, R.; et al. Ultrafast Hot-Hole Injection Modifies Hot-Electron Dynamics in Au/p-GaN Heterostructures. *Nat. Mater.* **2020**, *19* (12), 1312−1318.
(51) Tagliabue, G.; DuChene, J. S.; Habib, A.; Sundararaman, R.; Atwater, H. A. Hot-Hole versus Hot-Electron Transport at Cu/GaN Heterojunction Interfaces. *ACS Nano* **2020**, *14* (5), 5788−5797.
(52) Kim, S. J.; Thomann, I.; Park, J.; Kang, J.-H.; Vasudev, A. P.; Brongersma, M. L. Light Trapping for Solar Fuel Generation with Mie Resonances. *Nano Lett.* **2014**, *14* (3), 1446−1452.
(53) Zhang, Z.; Zhang, L.; Hedhili, M. N.; Zhang, H.; Wang, P. Plasmonic Gold Nanocrystals Coupled with Photonic Crystal Seamlessly on TiO_2 Nanotube Photoelectrodes for Efficient Visible Light Photoelectrochemical Water Splitting. *Nano Lett.* **2013**, *13* (1), 14−20.
(54) Zhao, Y.; Hoivik, N.; Wang, K. Microstructure and Photoelectric Response of Gold Nanocrystalline on TiO_2 Nanotube Arrays. *J. Phys. Chem. C* **2018**, *122* (14), 7877−7884.
(55) Dadgostar, S.; Tajabadi, F.; Taghavinia, N. Mesoporous Submicrometer TiO_2 Hollow Spheres As Scatterers in Dye-Sensitized Solar Cells. *ACS Appl. Mater. Interfaces* **2012**, *4* (6), 2964−2968.
(56) Tsai, M.-C.; Lee, J.-Y.; Chang, Y.-C.; Yang, M.-H.; Chen, T.-T.; Chang, I.-C.; Lee, P.-C.; Chiu, H.-T.; Lee, R.-K.; Lee, C.-Y. Scattering Resonance Enhanced Dye Absorption of Dye Sensitized Solar Cells at Optimized Hollow Structure Size. *J. Power Sources* **2014**, *268*, 1−6.
(57) Chen, Z.; Dinh, H. N.; Miller, E. *Photoelectrochemical Water Splitting*; Academic: New York, 2013.
(58) Shankar, K.; Mor, G. K.; Paulose, M.; Varghese, O. K.; Grimes, C. A. Effect of Device Geometry on the Performance of TiO_2 Nanotube Array-Organic Semiconductor Double Heterojunction Solar Cells. *J. Non-Cryst. Solids* **2008**, *354* (19), 2767−2771.
(59) Chen, F.; Ma, T.; Zhang, T.; Zhang, Y.; Huang, H. Atomic-Level Charge Separation Strategies in Semiconductor-Based Photocatalysts. *Adv. Mater.* **2021**, *33* (10), 2005256.
(60) Gao, S.; Zavabeti, A.; Wang, B.; Ren, R.; Yang, C.; Liu, Z.; Wang, Y. Nickel Phosphides Electrodeposited on TiO_2 Nanotube Arrays as Electrocatalysts for Hydrogen Evolution. *ACS Appl. Nano Mater.* **2021**, *4* (5), 4542−4551.
(61) Tian, H.; Shen, K.; Hu, X.; Qiao, L.; Zheng, W. N. S Co-Doped Graphene Quantum Dots-Graphene-TiO_2 Nanotubes Composite with Enhanced Photocatalytic Activity. *J. Alloys Compd.* **2017**, *691*, 369−377.

https://doi.org/10.1021/acs.jpcc.2c05893
J. Phys. Chem. C 2023, 127, 11−21

(62) Lei, Y.; Yang, Y.; Zhang, P.; Zhou, J.; Wu, J.; Li, K.; Wang, W.; Chen, L. Controllable One-Step Synthesis of Mixed-Phase TiO_2 Nanocrystals with Equivalent Anatase/Rutile Ratio for Enhanced Photocatalytic Performance. *Nanomaterials* **2021**, *11* (5), 1347.
(63) Thamaphat, K.; Limsuwan, P.; Ngotawornchai, B. Phase Characterization of TiO_2 Powder by XRD and TEM. *Agric. Nat. Resour* **2008**, *42* (5), 357−361.
(64) Sá, J.; Tagliabue, G.; Friedli, P.; Szlachetko, J.; Rittmann-Frank, M. H.; Santomauro, F. G.; Milne, C. J.; Sigg, H. Direct Observation of Charge Separation on Au Localized Surface Plasmons. *Energy Environ. Sci.* **2013**, *6* (12), 3584−3588.
(65) Xu, Z.; Lin, Y.; Yin, M.; Zhang, H.; Cheng, C.; Lu, L.; Xue, X.; Fan, H. J.; Chen, X.; Li, D. Understanding the Enhancement Mechanisms of Surface Plasmon-Mediated Photoelectrochemical Electrodes: A Case Study on Au Nanoparticle Decorated TiO_2 Nanotubes. *Adv. Mater. Interfaces* **2015**, *2* (13), 1500169.
(66) Subramanian, V.; Wolf, E. E.; Kamat, P. V. Catalysis with TiO_2/Gold Nanocomposites. Effect of Metal Particle Size on the Fermi Level Equilibration. *J. Am. Chem. Soc.* **2004**, *126* (15), 4943−4950.
(67) Hsu, C.; Shen, Y.; Wei, Z.; Liu, D.; Liu, F. Anatase TiO_2 Nanobelts with Plasmonic Au Decoration Exhibiting Efficient Charge Separation and Enhanced Activity. *J. Alloys Compd.* **2014**, *613*, 117−121.
(68) Ng, C.; Cadusch, J. J.; Dligatch, S.; Roberts, A.; Davis, T. J.; Mulvaney, P.; Gómez, D. E. Hot Carrier Extraction with Plasmonic Broadband Absorbers. *ACS Nano* **2016**, *10* (4), 4704−4711.
(69) Fromm, D. P.; Sundaramurthy, A.; Schuck, P. J.; Kino, G.; Moerner, W. E. Gap-Dependent Optical Coupling of Single "Bowtie" Nanoantennas Resonant in the Visible. *Nano Lett.* **2004**, *4* (5), 957−961.
(70) Jain, P. K.; El-Sayed, M. A. Plasmonic Coupling in Noble Metal Nanostructures. *Chem. Phys. Lett.* **2010**, *487* (4), 153−164.
(71) Bian, Z.; Tachikawa, T.; Zhang, P.; Fujitsuka, M.; Majima, T. Au/TiO_2 Superstructure-Based Plasmonic Photocatalysts Exhibiting Efficient Charge Separation and Unprecedented Activity. *J. Am. Chem. Soc.* **2014**, *136* (1), 458−465.
(72) Oh, K.; Dorcet, V.; Fabre, B.; Loget, G. Dissociating Water at N-Si Photoanodes Partially Covered with Fe Catalysts. *Adv. Energy Mater.* **2020**, *10* (3), 1902963.
(73) Kumtepe, A.; Altaf, C. T.; Sahsuvar, N. S.; Abdullayeva, N.; Koseoglu, E.; Sankir, M.; Sankir, N. D. Indium Sulfide Based Photoelectrodes for All-Vanadium Photoelectrochemical Redox Flow Batteries. *ACS Appl. Energy Mater.* **2020**, *3* (4), 3127−3133.
(74) Ding, Y.; Zhao, Y.; Li, Y.; Goodenough, J. B.; Yu, G. A High-Performance All-Metallocene-Based, Non-Aqueous Redox Flow Battery. *Energy Environ. Sci.* **2017**, *10* (2), 491−497.
(75) Cortés, E.; Wendisch, F. J.; Sortino, L.; Mancini, A.; Ezendam, S.; Saris, S.; de S. Menezes, L.; Tittl, A.; Ren, H.; Maier, S. A. Optical Metasurfaces for Energy Conversion. *Chem. Rev.* **2022**, *122*, 15082−15176.

https://doi.org/10.1021/acs.jpcc.2c05893
J. Phys. Chem. C 2023, 127, 11−21